Modeling inelasticity and failure in gold nanowires

Harold S. Park* and Jonathan A. Zimmerman†
Sandia National Laboratories, Livermore, California 94551, USA
(Received 5 March 2005; revised manuscript received 31 May 2005; published 2 August 2005)

We present numerical simulations of gold nanowires under tensile loading at various strain rates and wire sizes at room temperature. The simulations were performed using molecular dynamics modeling the gold nanowires using various forms of the embedded-atom method, and concentrated on investigating the yield and fracture properties of the nanowires. It is clearly demonstrated that the accurate modeling of stacking fault and surface energies is critical in capturing the fundamental deformation behavior of gold nanowires. By doing so, phenomena which have been observed both experimentally and numerically in first-principles calculations, such as the formation of atom-thick chains (ATCs) prior to fracture, zigzag, helical rotational motion of atoms within the ATCs, structural reorientation of the ATCs to a hexagonal crystal structure, and (111) faceting of the nanowire in the yielded neck region by the ATCs, are accurately captured.

DOI: 10.1103/PhysRevB.72.054106 PACS number(s): 61.46.+w, 62.25.+g

I. INTRODUCTION

The study of nanometer-scale mechanical building blocks has intensified dramatically within the past decade to take advantage of the improved mechanical properties brought about by the relative smallness of nanostructured materials. Within the subset of nanostructured materials, nanowires have emerged as an important structural component in future nanomaterials mainly due to their high strength and ductility as compared to bulk materials. Many potentially important applications and devices involving nanowires at a fundamental structural level have been proposed. For example, nanowires are envisioned as being suitable as junctions in electronic circuits, structural reinforcements in composite materials, general building blocks for logic and memory circuits, and as sensors to detect airborne biological and chemical toxins. We refer the interested reader to the reviews of Lieber[1] and Kovtyukhova and Mallouk[2] for further details.

Experimental work has been performed by many researchers characterizing the electrical, mechanical, and thermal properties of various metallic nanowires. In particular, we note the work of Landman *et al.*,[3] Takayanagi and co-workers,[4–6] Brandbyge *et al.*,[7] Rubio *et al.*,[8] and Rodrigues and Ugarte.[9] These experiments have revealed many of the interesting physics governing the behavior of nanowires, in particular that the wire cross-sectional area often reduces to that of a single-atom thickness prior to failure under tensile loading, and that the conductance and mechanical deformation of the nanowires are tightly coupled. The stability of the single-atom chain has also been studied analytically by Torres and co-workers,[10] and Zhang *et al.*;[11] the effects of nanowire orientation on wire stability was studied using Monte Carlo simulations by Jagla and Tosatti.[12]

Computer simulations have also been performed analyzing the deformation behavior of metallic nanowires. The first-principles simulations of Sanchez-Portal *et al.*[13] were unique in that they reported that gold nanowires assume a zigzag-type shape with two atoms per unit cell under tensile loading conditions. The effects of surface stress driven reorientations was studied extensively by Diao *et al.*,[14,15] while the phenomena of amorphization at strain rates typically above 10^{10} s^{-1} was reported by Ikeda *et al.*[16] for nickel nanowires. The deformation behavior of metallic nanowires has been studied previously using first-principles simulations by Mehrez and Ciraci[17] and da Silva *et al.*,[18] while molecular dynamics (MD) simulations of nanowire failure were performed by Wu *et al.*,[19] Walsh *et al.*,[20] Kang and Hwang,[21] and Liang and Zhou.[22]

There are two major objectives of this paper. The first is to analyze the tensile failure of gold nanowires through MD simulations using the embedded-atom method (EAM).[23] By comparing results obtained using two EAM potentials which have been fitted to the same functional forms, the importance of accurately modeling the stacking fault and surface energies of nanowires in order to capture deformation phenomena observed experimentally and in first-principles simulations has been determined. By utilizing an EAM potential that obeys the above characteristics, it is found that under tensile loading, a three-atom-thick chain (ATC) is formed which can extend to lengths of 10 nm. The motion of the atoms within the ATC follows a zigzag, helical path that has been observed in previously reported experiments[4] and first principles simulations.[13,17] The same ATC can, by gradually reducing the applied loading rate to zero and fixing the resulting wire length, form a stable, reoriented hexagonal crystal structure that is comprised of two parallel (111) atomic planes; this type of structural transition from (001) to (111) at exposed free surfaces has been observed experimentally by Kondo *et al.*[5] and numerically using MD simulations by Hasmy and Medina.[24] Outside the ATC in the necked region of the nanowires, (111) faceting of the atomic planes is found to match the experimental observations of Kondo and Takanayagi.[25]

The second thrust is to fully characterize the yield and fracture properties of gold nanowires. Previous works[19,22,26,27] have analyzed the behavior of metallic nanowires until yield; however, a thorough characterization of the yield and fracture properties of nanowires has not been previously reported to our knowledge. In this work, the yield and fracture properties of gold nanowires are determined by varying the loading rate and cross-sectional areas of the wires.

TABLE I. Properties of Voter-Chen and Foiles potentials compared to experimental data.

Property	Voter-Chen	Foiles	Experiment
a_0 (Å)	4.08	4.08	4.08 (Ref. 31)
E_{coh} (eV)	3.93	3.93	3.93 (Ref. 31)
B (GPa)	166.67	166.67	166.67 (Ref. 31)
Z	79	79	79
Mass (amu)	196.97	196.97	196.97
C_{11} (GPa)	188	185.8	186
C_{12} (GPa)	156	157.1	157
C_{44} (GPa)	42	38.949	42
γ_{110} (mJ/m^2)	969	1309	1700 (Ref. 32)
γ_{111} (mJ/m^2)	769	1090	1040 (Ref. 33)
γ_{100} (mJ/m^2)	892	1180	1444 (Ref. 34)
E_{vf} (eV)	0.9	0.97	0.9/0.95
γ_{sf} (mJ/m^2)	9.74	31	32

II. SIMULATION METHODS

The MD simulations performed in this work used the embedded atom method[23] as the underlying atomic interaction model. For the EAM, the total energy U for a system of atoms can be written as

$$U = \sum_{i}^{N} \left(F_i(\bar{\rho}_i) + \frac{1}{2} \sum_{j \neq i}^{N} \phi_{ij}(R_{ij}) \right) \tag{1}$$

where the summations in Eq. (1) extend over the total number of atoms N in the system, F_i is the embedding function, $\bar{\rho}_i$ is the electron density at atom i, ϕ_{ij} is a pair interaction function, and R_{ij} is the distance between atoms i and j.

Two EAM potentials were utilized for this work. The first is the potential developed by Voter and Chen[28,29] and was fitted to cohesive energy, equilibrium lattice constant, bulk modulus, cubic elastic constants, and the unrelaxed vacancy formation energy, bond length, and bond strength of the diatomic molecule. The second potential was developed by Foiles and utilizes the same functional forms as the Voter-Chen potential with parameters modified to yield a more accurate estimate of the intrinsic stacking-fault energy.[30] The only difference in functional form between the two potentials is in the expression utilized to calculate the electron density. For the Voter-Chen potential, the expression used was

$$\rho(r) = r^6(e^{-\beta_M r} + 2^9 e^{-2\beta_M r}) \tag{2}$$

while for the Foiles potential, we used

$$\rho(r) = r^8(e^{-\beta_M r} + 2^{11} e^{-2\beta_M r}). \tag{3}$$

The embedding function $F_i(\bar{\rho}_i)$ was fitted to the universal energy form of Rose *et al.*[31] for both potentials. A full listing of the physical properties and fitting parameters that characterize both the Voter-Chen and Foiles potential are found in Tables I and II.

The generalized stacking fault curves for the Voter-Chen and Foiles potentials are shown in Fig. 1. As can be seen, the unstable stacking-fault energies of both potentials are quite similar, with the Voter-Chen potential being slightly more ductile. However, compared to the experimentally observed value for the stacking-fault energy of 32 mJ/m^2 for gold, the Voter-Chen potential predicts a value of 9.74 mJ/m^2, while the Foiles model predicts a more accurate value of 31 mJ/m^2. The ramifications of this discrepancy will be discussed later in reference to the simulation results. A thorough discussion on the importance of correctly capturing stacking fault energies can be found in Zimmerman *et al.*[35]

TABLE II. Fitting parameters for Voter-Chen and Foiles potentials.

Parameter	Voter-Chen	Foiles
m	20	20
g	−3.3	0.0
r_{cut} (Å)	5.5155	5.6
β_M (1/Å)	3.6967	3.18783126
α_M (1/Å)[a]	1.8964	1.2031576
D_M (eV)[a]	0.6748	0.6569397
R_M (Å)[a]	2.5686	2.5471737

[a]Fitting parameters for Morse pair potential $\phi_{ij}(R_{ij})$ in (1).

Square-cross-section gold [100] nanowires were created out of a bulk fcc crystal with initial surface orientations of [100], [010], and [001]. The wires were all 16 nm long, with varying cross-sectional lengths of 2.588, 3.66, and 5.176 nm. The wires were first relaxed to an equilibrium minimum-energy configuration with free boundaries everywhere, and then thermally equilibrated to 300 K for 20 ps using a Nosé-Hoover thermostat[36,37] with a time step of 0.001 ps while keeping the length of the wires constant. The thermostat was removed prior to loading, ensuring adiabatic loading conditions; no periodic boundary conditions were utilized at any stage in the simulations.

The applied strain rates for each nanowire were 3×10^7, 3×10^8, 3×10^9, and 3×10^{10} s^{-1} along with an incremental quasistatic simulation for each wire. The nanowires were

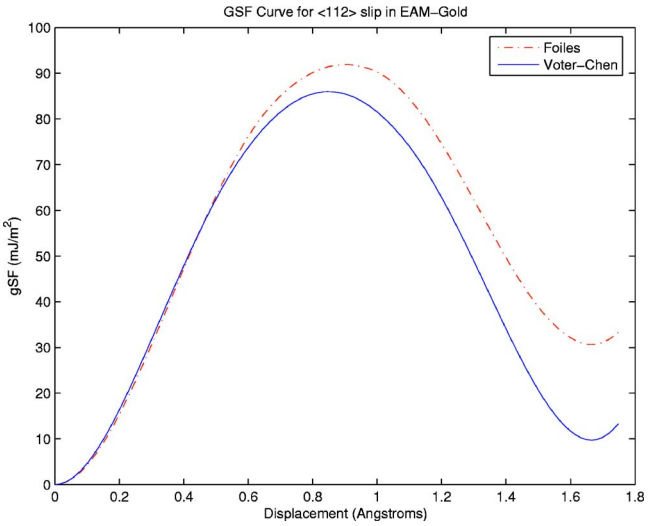

FIG. 1. (Color online) Generalized stacking-fault curves for Foiles and Voter-Chen potentials.

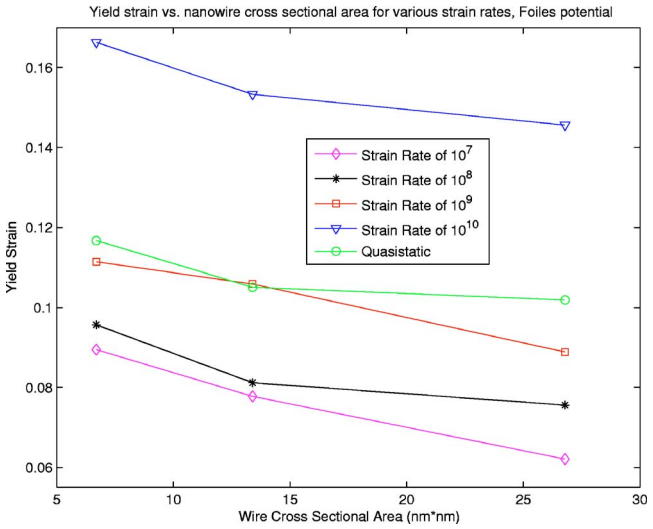

FIG. 2. (Color online) Yield strain as a function of wire area for various strain rates.

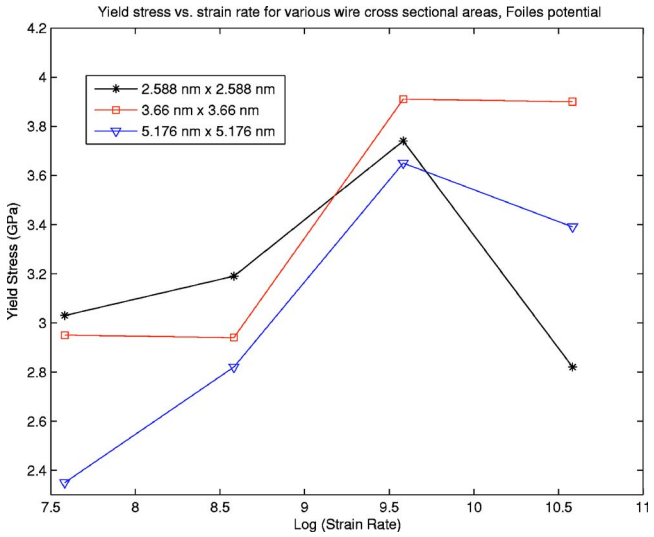

FIG. 4. (Color online) Yield stress as a function of strain rate for wires of various cross-sectional areas.

loaded in tension in the [100] direction by fixing one end of the wire, creating a ramp velocity profile which went from zero at the fixed end to a maximum value at the free end, then pulling the free end at the maximum value. The ramp velocity profile was utilized to avoid the emission of shock waves from the loading end of the wire. The equations of motion were integrated in time using a velocity Verlet algorithm, and all simulations were performed using the Sandia-developed code WARP.[38–40]

III. SIMULATION RESULTS AND DISCUSSION

A. Mechanical properties

The results of the nanowire mechanical properties such as yield strain, yield stress, and fracture strain as functions of the wire cross-sectional area and loading rate are shown in Figs. 2–6 for the Foiles potential. Similar results for the Voter-Chen potential in comparison to the Foiles potential will be summarized later in this section.

Strain is defined as $\epsilon=(l-l_0)/l_0$, where l is the current wire length and l_0 is the wire length after the energy-minimizing relaxation process. Yield strain is defined as the strain at which the maximum tensile stress occurs, while fracture strain is defined as the strain at which the wire breaks into two distinct entities. The stresses reported in this work were calculated using the virial theorem, which takes the form

$$\sigma_{ij}=\frac{1}{V}\left(\frac{1}{2}\sum_{\alpha=1}^{N}\sum_{\beta\neq\alpha}^{N}U'(r^{\alpha\beta})\frac{\Delta x_i^{\alpha\beta}\Delta x_j^{\alpha\beta}}{r^{\alpha\beta}}-\sum_{\alpha=1}^{N}m_\alpha\dot{x}_i^\alpha\dot{x}_j^\alpha\right) \quad (4)$$

where V is the current volume of the nanowire, N is the total number of atoms, $\dot{x}_i^\alpha$ is the ith component of velocity of atom

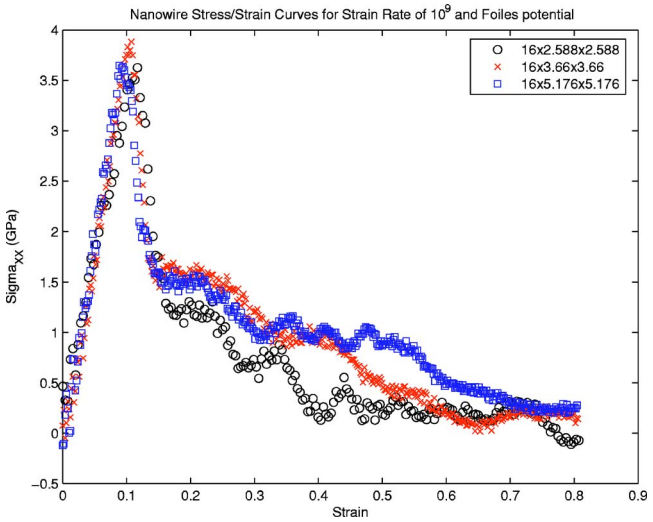

FIG. 3. (Color online) Stress-strain curves for nanowires loaded at a strain rate of 10^9 s^{-1} using the Foiles potential.

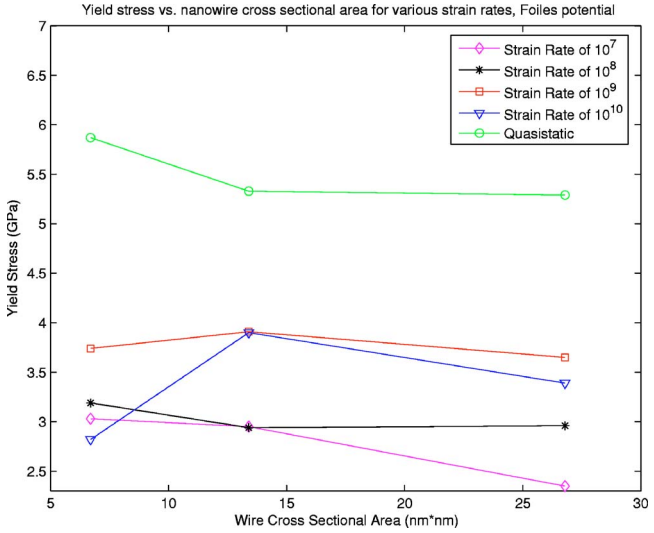

FIG. 5. (Color online) Yield stress as a function of cross-sectional area for various strain rates.

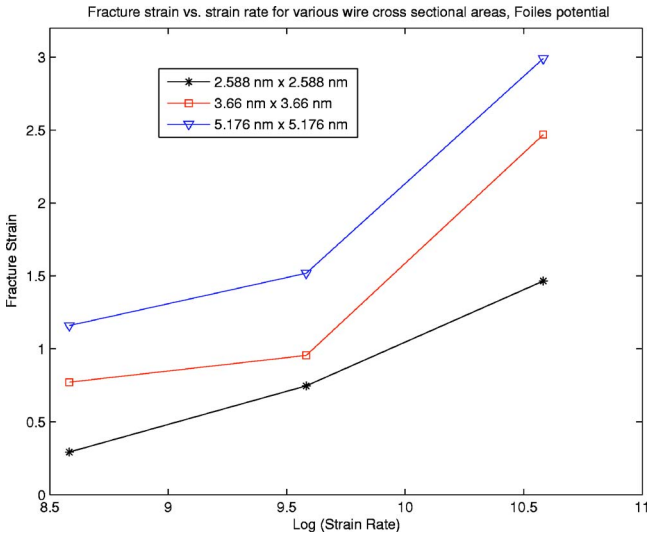

FIG. 6. (Color online) Fracture strain as a function of strain rate for various wire cross-sectional areas.

α, m_α is the mass of atom α, $r^{\alpha\beta}$ is the distance between two atoms α and β, $\Delta x_j^{\alpha\beta}=x_j^\alpha-x_j^\beta$, U is the potential energy function, and $r^{\alpha\beta}=\|\Delta x_j^{\alpha\beta}\|$.

As can be seen in Fig. 2, the yield strain increases with decreasing wire cross-sectional area for all applied strain rates. This appears to support the notion that while smaller wires have a larger ratio of surface area to volume, larger wires are more prone to slip and dislocation initiation from free surfaces because of the increase in overall surface area. However, Diao *et al.*[41] have noted that this increase in yield strain is due to the fact that smaller wires relax more initially, thus requiring a larger extension to overcome the compressive stress state in the wire core. We note that the elastic portion of the stress-strain curve is linear for all strain rates and wire sizes considered; an example of the stress-strain curves for all wires loaded at a strain rate of 10^9 s^{-1} using the Foiles potential is shown in Fig. 3.

Figure 4 shows the yield stress as a function of strain rate for wires of various cross sectional area. As can be seen, the smallest wire of cross sectional length 2.588 nm has the largest yield stress for strain rates lower than 10^9 s^{-1}. Figure 5 shows the yield stress as a function of cross-sectional area for various strain rates, and demonstrates that the yield strength of a given wire increases with decreasing cross-sectional area for strain rates below 10^9 s^{-1}. The yield strength of the wires at the strain rate of 10^9 s^{-1} is fairly similar, while at strain rates around 10^{10} s^{-1}, the smallest wires are the weakest.

Because the trend found above that the yield strength decreases at high strain rates opposes results reported in the literature,[19,22] a careful analysis of the virial stress in Eq. (4) was conducted. It was found that the ramp velocities that are initially applied to the wires at strain rates of 10^{10} s^{-1} are large enough such that the kinetic portion of the virial stress (4) is of the same order of magnitude as the overall stress, causing the initial stress to be artificially compressive. If the total amount of stress increase is measured for the $\dot{\epsilon}=10^{10}$ s^{-1} simulations, it was found that the yield stress is larger for those strain rates (4.6–6.4 GPa) than for the lower strain rates for all wires.

The fracture strain as a function of strain rate for each wire is plotted in Fig. 6. In general, the fracture strain increases with wire cross-sectional area for a given strain rate. Furthermore, the fracture strain increases with strain rate for all wire cross sectional areas considered, indicating the existence of a strain rate hardening mechanism in the wires.

The dramatic effects of high strain rate loading upon the nanowire mechanical behavior are illustrated in Figs. 2 and 6, where the yield strain and fracture strain of the wires loaded at strain rates of 10^{10} s^{-1} increase markedly over those wires loaded at lower strain rates. This agrees with the analysis of Ikeda *et al.*,[16] who showed that high strain-rate loading transforms the deformation process from one of crystalline slip to that of homogeneous flow characteristic of a fluid. The resulting ductility in the wires is fairly dramatic; Fig. 6 shows that the largest wires elongate to almost three times their original length before fracture at such elevated strain rates.

An interesting trend can be seen in Figs. 2 and 5, which show that the quasistatically loaded nanowires have yield strains and stresses that appear to outstrip all dynamically loaded wires with the exception of the wires loaded at strain rates of 10^{10} s^{-1}. The quasistatically loaded wires yield at higher strains and stresses because the atoms within the wire are allowed to relax back to energy-minimizing positions after each load increment is applied. This is in contrast to the dynamic simulations, in which the atomic motion is purely in response to the applied load; in essence, atoms in a dynamic simulation are not afforded the relaxation time that atoms loaded quasistatically are, and thus the dynamically loaded wires yield at smaller strains and yield stresses than the quasistatically loaded wires.

The above analysis was also performed for the same size nanowires using the Voter-Chen potential. Similar trends were observed in all cases; due to the fact that the Voter-Chen potential is more ductile than the Foiles potential due to the lower stacking-fault energies and surface energies, the fracture strains and yield strains were lower in most cases using the Voter-Chen potential.

The typical deformation process for a nanowire is shown in Fig. 7. This figure corresponds to the 2.588 nm Foiles nanowire loaded at a strain rate of 10^9 s^{-1}. Similar results are seen at lower strain rates, while at higher strain rates the wires fail in a ductile manner brought on by amorphization as seen in Refs. 16 and 42. As can be seen, the nanowires experience clearly defined stages of deformation, including yield and the onset of necking. The necking process develops into a three-atom-thick chain seen in Fig. 7; thin wire necks of similar thickness have been reported experimentally by many groups.[3–9] For the simulations reported here, the ATC within the wire neck gradually elongates under continued tensile loading for up to 85 ps until fracture occurs. It is found that the ATC may extend to a maximum length of 10 nm prior to fracture. Further analysis of the ATC is given in the next section.

In contrast to the inelastic nanowire response observed for the Foiles potential, the inelastic behavior for the Voter-Chen potential differs dramatically, as seen in Fig. 8. For example,

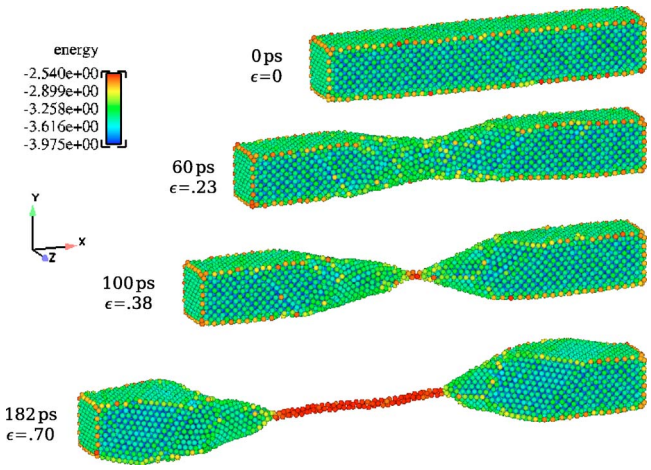

FIG. 7. (Color online) Snapshots of the deformation of the 2.588 nm wire at a strain rate of 3×10^9 s^{-1} using the Foiles potential (Ref. 30). Atoms are colored according to their value of potential energy.

yield occurs at two distinct areas along the wire length as seen in Fig. 8 when $\epsilon=0.13$. Furthermore, stacking faults and surface steps are clearly visible in the Voter-Chen wire, whereas they are not seen in the Foiles wire. A small ATC forms briefly in the Voter-Chen wire immediately preceding fracture, but does not fully develop like the one seen in the Foiles wire, and fractures shortly after the formation of the ATC. The competition between the two yielded regions in the Voter-Chen wire is believed to prevent the localized necking and subsequent formation of the ATC as seen in the Foiles wire.

Another striking difference between the nanowire response for the two potentials is in the (111)-type faceting of atomic planes which is observed most clearly at $\epsilon=0.70$ in Fig. 7. This type of faceting for [100] nanowires has been observed experimentally by Kondo and Takanayagi.[25] The existence of such faceting of (111) planes is difficult to ob-

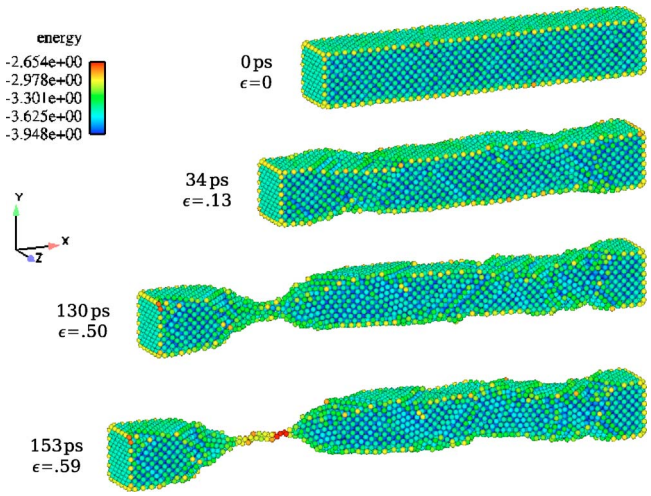

FIG. 8. (Color online) Snapshots of the deformation of the 2.588 nm wire at a strain rate of 3×10^9 s^{-1} using the Voter-Chen potential (Ref. 29). Atoms are colored according to their value of potential energy.

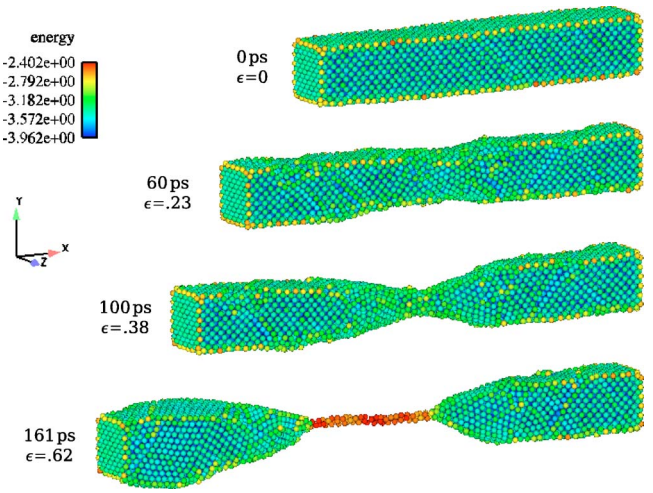

FIG. 9. (Color online) Snapshots of the deformation of the 2.588 nm wire at a strain rate of 3×10^9 s^{-1} using the Foiles potential (Ref. 30) and the uniform scaling of coordinate loading condition. Atoms are colored according to their value of potential energy.

serve in the Voter-Chen wire. The faceted (111) planes and the ATC are markedly similar to the "disordered" region seen in Ref. 25. In the simulations presented here, the ATC elongates by incorporating atoms which lie in the disordered region after initial necking occurs. The faceted (111) planes serve as the boundary between the disordered region and the remainder of the wire, and prevent atoms outside the disordered region from entering the ATC, a fact also noted by Kondo and Takanayagi.[25]

The distinct postyield behavior between the Foiles and Voter-Chen nanowires can be simply explained due to the fact that both potentials were fitted to the same functional forms and fitting parameters. As can be seen in Table I, the major differences between the Foiles and Voter-Chen potentials lie in the accurate representation of the stacking-fault and surface energies for gold. The low stacking-fault energy for the Voter-Chen potential results in an overly ductile yield behavior, resulting in premature dislocation emission and plasticity. Because both the Foiles and Voter-Chen potentials were fitted to similar functional forms, this underscores the importance of accurately modeling the stacking-fault energy when modeling atomic-scale plasticity.

We close this section by commenting on the relationship between the formation of the ATC and the type of ramp velocity loading condition employed for the simulations in this paper. In MD simulations of the tensile response of nanowires, the most commonly utilized loading described in the literature is that of uniform scaling of coordinates. It might be presumed that the extra initial kinetic energy given to the atoms via the ramp loading utilized in this work would contribute to an artificially energetic phase space. Therefore, a benchmark simulation was performed on the 2.588 nm nanowire using a uniform scaling of coordinates at a strain rate of 10^9 s^{-1} to see if similar behavior was observed.

As can be seen in Fig. 9, similar to the ramp velocity loading case, yield followed by formation of an ATC was observed in the 2.588 nm nanowire deformed by the uniform scaling of coordinates. While the response of the nanowire

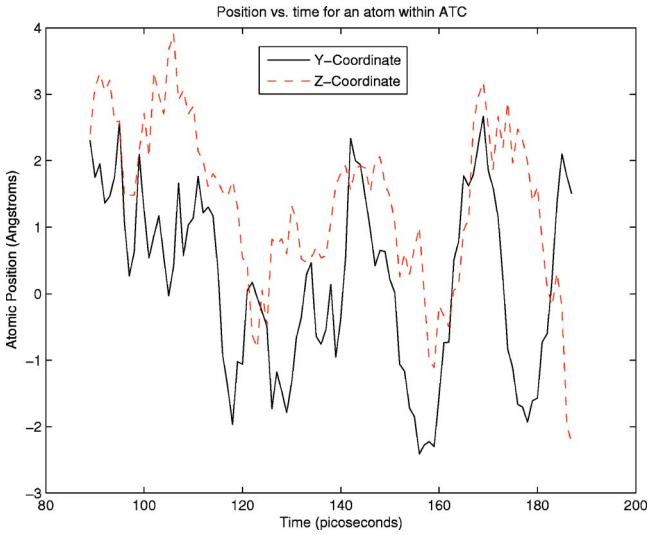

FIG. 10. (Color online) Time history of the y and z coordinates of an atom within the ATC shown in Fig. 7.

differs under the two different loading conditions, the key physical features of the nanowire, namely, the formation of the ATC and faceting of the (111) atomic planes surrounding the ATC, are found to match in both cases, indicating that the physical phenomena observed are not artificially created by the type of loading condition utilized.

B. Analysis of the ATC

The behavior of the ATC within the Foiles wire neck with the ramp velocity loading was investigated by tracking the position of an atom within the chain from the point at which the ATC formed until fracture of the chain occurred. The y and z coordinates of the atom as functions of time are shown in Fig. 10, while the radius of motion perpendicular to the loading direction is shown in Fig. 11. The y and z coordinates are chosen because the x direction constitutes the loading direction.

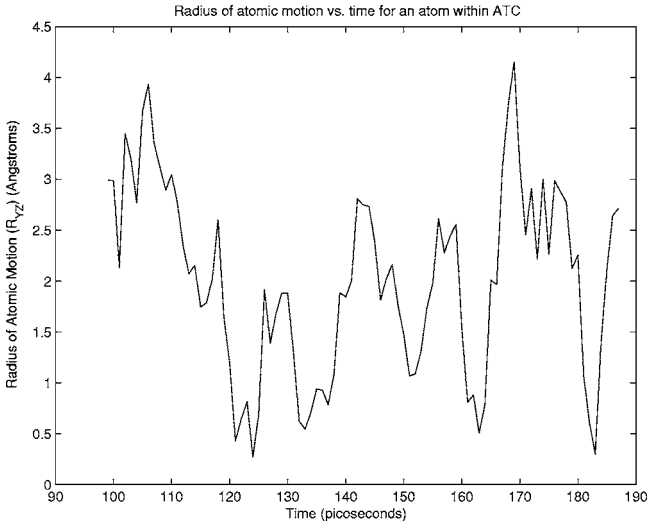

FIG. 11. Time history of the radial motion of an atom within the ATC shown in Fig. 7.

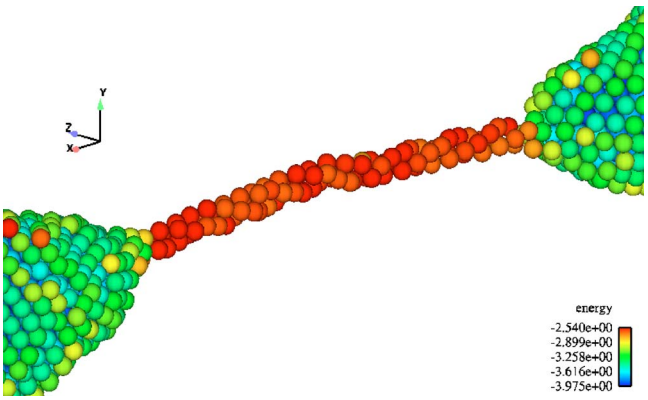

FIG. 12. (Color online) Illustration of the helical, zigzag structure within the ATC. Atoms are colored according to their value of potential energy.

From the formation of the ATC at about 100 ps, Figs. 10 and 11 show the motion of the atom to follow a spinning, rotational path as the tensile deformation continues. This deformation pattern closely resembles the zigzag, helical pattern of deformation first reported by Sanchez-Portal *et al.*[13] for first-principles simulations of nanowires under tensile loading, and concurs with the rotational path of deformation described by Mehrez and Ciraci.[17] Such a helical atomic arrangement for very thin nanowires has been reported experimentally by Kondo and Takanayagi,[4] and using genetic MD algorithms by Wang *et al.*[43] The helical, zigzag structure of the ATC is shown clearly in Fig. 12.

Due to the large amount of deformation the wire has undergone, the atoms within the ATC have low coordination numbers. Because of this fact and because the wire is under perpetual loading, the atoms within the ATC, while preferring to create highly packed reoriented surface structures (see below), are unable to do so and remain in an unstable equilibrium. Thus, the atoms within the ATC instead move in a rotational, zigzag path along which perpetually attempt to maximize close packing and acquire more atomic bonds are made.

The stability and behavior of the ATC within the wire neck was evaluated for purposes of comparing against experimentally reported studies of extended stable ATCs and nanobridges.[25,44] To accomplish this within the MD simulations, the loading velocity on the 2.588 nm Foiles nanowire loaded at a strain rate of 10^9 s^{-1} was gradually reduced by 0.01 lattice unit per picosecond (0.0407 Å/ps) every picosecond starting at a simulation time of 120 ps until the loading rate on the wire had decreased to zero at 134 ps. The gradual reduction of loading rate over time was designed to minimize the effects of any shocks that could result from an overly quick reduction of the loading rate. At the simulation time of 134 ps when the loading rate had been reduced to zero, the wire was fixed at both ends.

Figure 13 shows the time evolution of the ATC after the loading rate was ramped down to zero and both ends of the wire were fixed. As can be seen, the initially disordered ATC reaches a lower-energy equilibrated state after about 160 ps. It is found that the same equilibrated ATC continues to remain stable for over 1000 ps. It is expected that the wire and

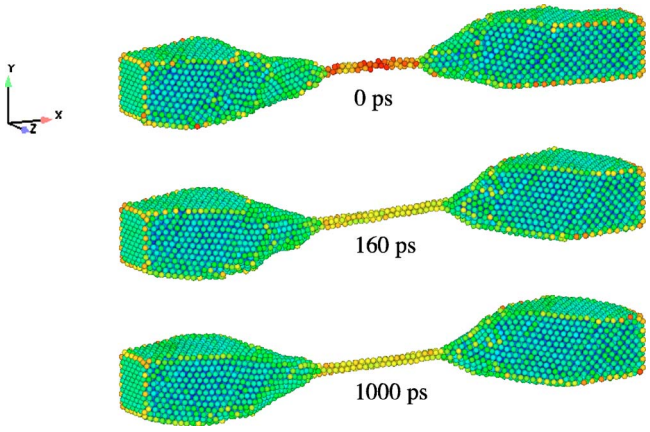

FIG. 13. (Color online) Snapshots of the ATC in the 2.588 nm wire after the loading rate has been reduced to zero and both ends of the wire have been fixed at a strain of $\epsilon=0.47$. Atoms are colored according to their value of potential energy.

ATC would remain indefinitely stable in the equilibrated configuration shown in Fig. 13.

More interestingly, close-up snapshots of the ATC are shown in Fig. 14. As can be seen, the initial fcc structure of the wire surfaces has been altered to form a stable, hexagonal lattice structure. The ATC contains three atomic rows, and can be seen to consist of two parallel (111) atomic planes. The faceting of (111)-type planes outside the necked region containing the ATC is again seen clearly in Fig. 13. There, it can be seen upon equilibration that (111) faceting has occurred on both sides of the stabilized ATC, again in agreement with the experiments of Kondo and Takanayagi.[25]

This reorientation from bulk (001) fcc to hexagonal (111) structure corresponds with experimental and numerical predictions, for example, as seen experimentally in the work of Kondo *et al.*[5] and in the MD simulations of Hasmy and Medina,[24] and results from an attempt to maximize close-packing and to reduce surface energy within the ATC. In

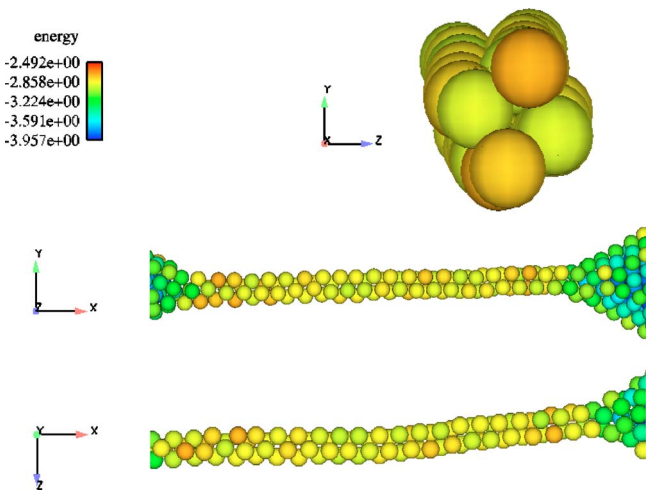

FIG. 14. (Color online) Close-up snapshots of the ATC in the 2.588 nm wire from various perspectives indicating the reoriented hexagonal structure of the stable ATC. Atoms are colored according to their value of potential energy.

experiments,[25,44] such ATCs have been observed predominantly in [110]-oriented nanowires. Therefore, a simulation of an initially [110]-oriented wire was performed, and it was found that using the Foiles potential an ATC of identical structure formed upon gradual relaxation of load as described earlier. With the Voter-Chen potential, again a short ATC formed briefly, but then fractured soon after. Details of the [110]-oriented nanowire simulations will be presented in a subsequent publication.[45]

IV. CONCLUSIONS

The tensile failure of gold nanowires was investigated using MD with two different EAM potentials at room temperature. In doing so, the importance of accurately capturing the stacking-fault and surface energies of the nanowire was revealed by comparing results from two different EAM potentials which had been fit using the same functional forms. Due to the fact that the stacking-fault and surface energies are very low for the Voter-Chen potential, the tensile deformation of Voter-Chen gold nanowires was observed to be overly ductile, thus hindering the development of ATCs typically seen in gold nanowires.

In contrast, the Foiles potential provided much more accurate measurements of both the stacking fault and surface energies. Thus, during the tensile failure process, an elongated ATC is found to form; the atoms within the ATC are found to exhibit behavior similar to that observed in first-principles calculations by Sanchez-Portal *et al.*,[13] in that a spinning, rotational path of motion is observed for a helical, zigzag-structured ATC. Very thin nanowires have also been experimentally observed to form a helical structure by Kondo and Takanayagi.[4] The faceted (111) planes surrounding the necked region and ATC match experimental predictions by Kondo and Takanayagi,[25] who observed faceted (111) planes surrounding a region of disorder in [100] gold nanowires.

Furthermore, the ATC is found to equilibrate into an elongated, stable chain of atoms after the loading rate has been reduced to zero and wire length fixed from an initial (100) orientation to a (111) orientation, which matches the experimental results of Kondo *et al.*[5] and the numerical simulations of Hasmy and Medina,[24] Finally, faceting of (111) planes in the neck region surrounding the ATC is again found to match the experimental predictions of Kondo and Takanayagi.[25]

In addition, the loading rates and cross-sectional areas of the nanowires were varied to perform a comprehensive analysis of the yield and fracture properties of the nanowires. In general, the yield strain is found to increase with decreasing wire cross-sectional area, while the fracture strain is found to increase with both increasing cross-sectional area and loading rate. At strain rates below 10^9 s^{-1}, yield stress is found to increase with decreasing cross-sectional area, while the results are inconsistent at higher strain rates. One major reason for this is due to the fact that the initial ramp velocity loading of the nanowires at high strain rates is large enough that it creates an artificially compressive initial stress state as defined by the virial theorem (4). Finally, strain-rate hardening effects are found, as the yield stress tends to increase with increasing strain rate.

As with any MD simulation, we note that the strain rates used for the simulations shown are considerably higher than those seen in actual experiment. The simulations demonstrated that the strongest wires were those loaded quasistatically; the weakest were those loaded at the lowest strain rate of 10^7 s^{-1}. The increasing yield strength with strain rate can be attributed to the effects of phonon drag, which impedes dislocation nucleation with increasing strain rate. In contrast, the high strength of the quasistatically loaded nanowire as compared to the dynamically loaded nanowires occurs because the wires remain relatively pristine prior to the onset of plasticity as the atoms are allowed to relax back to energy-minimizing configurations after each load increment.

It therefore appears that an idealized quasistatic tensile deformation increases the yield stress more than the effect of phonon drag at high strain rates, excluding, of course amorphization at strain rates around $\dot{\epsilon} \approx 10^{10}$ s^{-1}.[16] While the effects of phonon drag may be mitigated at strain rates lower than $\dot{\epsilon} = 10^7$ s^{-1}, other factors will become active between strain rates of $\dot{\epsilon} = 10^{-2} - 10^6$ s^{-1} that may tend to either promote or shield the strain-rate-hardening mechanisms observed at higher strain rates. As this transition strain-rate region is currently not well understood, and is inaccessible by direct MD simulations, techniques are being developed to study atomistic behavior at low strain rates; we point interested readers to the review of Voter *et al.*[46]

We also note that the results for the ATC have been obtained using empirical potentials which are generally not fitted for low-coordination structures. However, the fact that the structure and form of the ATC qualitatively match those found in experiment[25] indicates that carefully constructed empirical potentials that can accurately model atomic-scale plasticity are capable of modeling complex deformation in the absence of more accurate first-principles simulation results.

Future work needs to be performed to analyze the effect of temperature upon the basic mechanical properties of the nanowires, as the wires are envisioned to have many potential applications in electrical circuits and interconnects. Of related interest, due to the experimentally reported variety in wire behavior under different orientations, the synthesis process for the wires should be thoroughly investigated, such that a clear understanding between synthesis and mechanical properties can be established for design purposes.

ACKNOWLEDGMENTS

We would like to thank E. Dave Reedy and Neville R. Moody for their support of this research. We would also like to thank Stephen M. Foiles for his help with characterizing the EAM potential and Gregory J. Wagner for his assistance with using the WARP code. Sandia is a multiprogram laboratory operated by Sandia Corporation, a Lockheed Martin Company, for the United States Department of Energys National Nuclear Security Administration under Contract No. DE-AC04-94AL85000.

*Present address: Department of Civil and Environmental Engineering, Vanderbilt University, Nashville, TN 37235. Electronic address: hpark@alumni.northwestern.edu

†Electronic address: jzimmer@sandia.gov

[1] C. M. Lieber, MRS Bull. **28**, 486 (2003).

[2] N. I. Kovtyukhova and T. E. Mallouk, Chem.-Eur. J. **8**, 4355 (2002).

[3] U. Landman, W. D. Luedtke, N. A. Burnham, and R. J. Colton, Science **248**, 454 (1990).

[4] Y. Kondo and K. Takayanagi, Science **289**, 606 (2000).

[5] Y. Kondo, Q. Ru, and K. Takayanagi, Phys. Rev. Lett. **82**, 751 (1999).

[6] H. Ohnishi, Y. Kondo, and K. Takayanagi, Nature (London) **395**, 780 (1998).

[7] M. Brandbyge, J. Schiotz, M. R. Sorensen, P. Stoltze, K. W. Jacobsen, J. K. Norskov, L. Olesen, E. Laegsgaard, I. Stensgaard, and F. Besenbacher, Phys. Rev. B **52**, 8499 (1995).

[8] G. Rubio, N. Agrait, and S. Vieira, Phys. Rev. Lett. **76**, 2302 (1996).

[9] V. Rodrigues and D. Ugarte, Phys. Rev. B **63**, 073405 (2001).

[10] J. A. Torres, E. Tosatti, A. D. Corso, F. Ercolessi, J. J. Kohanoff, F. D. D. Tolla, and J. M. Soler, Surf. Sci. Lett. **426**, L441 (1999).

[11] C.-H. Zhang, F. Kassubek, and C. A. Stafford, Phys. Rev. B **68**, 165414 (2003).

[12] E. A. Jagla and E. Tosatti, Phys. Rev. B **64**, 205412 (2001).

[13] D. Sanchez-Portal, E. Artacho, J. Junquera, P. Ordejon, A. Garcia, and J. M. Soler, Phys. Rev. Lett. **83**, 3884 (1999).

[14] J. Diao, K. Gall, and M. L. Dunn, Nat. Mater. **2**, 656 (2003).

[15] J. Diao, K. Gall, and M. L. Dunn, Phys. Rev. B **70**, 075413 (2004).

[16] H. Ikeda, Y. Qi, T. Cagin, K. Samwer, W. L. Johnson, and William A. Goddard III, Phys. Rev. Lett. **82**, 2900 (1999).

[17] H. Mehrez and S. Ciraci, Phys. Rev. B **56**, 12632 (1997).

[18] E. Z. da Silva, A. J. R. da Silva, and A. Fazzio, Phys. Rev. Lett. **87**, 256102 (2001).

[19] H. A. Wu, A. K. Soh, X. X. Wang, and Z. H. Sun, Key Eng. Mater. **261-263**, 33 (2004).

[20] P. Walsh, W. Li, R. K. Kalia, A. Nakano, P. Vashista, and S. Saini, Appl. Phys. Lett. **78**, 3328 (2001).

[21] J.-W. Kang and H.-J. Hwang, Nanotechnology **12**, 295 (2001).

[22] W. Liang and M. Zhou, in Proceedings of the Institution of Mechanical Engineers, Part C [J. Mech. Eng. Sci. 218, 599 (2004)].

[23] M. S. Daw and M. I. Baskes, Phys. Rev. B **29**, 6443 (1984).

[24] A. Hasmy and E. Medina, Phys. Rev. Lett. **88**, 096103 (2002).

[25] Y. Kondo and K. Takayanagi, Phys. Rev. Lett. **79**, 3455 (1997).

[26] K. Gall, J. Diao, and M. L. Dunn, Nano Lett. **4**, 2431 (2004).

[27] J. Diao, K. Gall, and M. L. Dunn, Nano Lett. **4**, 1863 (2004).

[28] A. F. Voter and S. P. Chen, in *Characterization of Defects in Materials*, edited by R. W. Siegel, J. R. Weertman, and R. Sinclair, Mater. Res. Soc. Symp. Proc. No. 82 (Materials Research Society, Pittsburgh, 1987), p. 175.

[29] A. F. Voter, Los Alamos Unclassified Technical Report No. LA-UR 93-3901, 1993 (unpublished).

[30] S. M. Foiles (private communication).
[31] J. H. Rose, J. R. Smith, F. Guinea, and J. Ferrante, Phys. Rev. B **29**, 2963 (1984).
[32] L. Vitos, A. V. Ruban, H. L. Skriver, and J. Kollar, Surf. Sci. **411**, 186 (1998).
[33] N. Takeuchi, C. T. Chan, and K. M. Ho, Phys. Rev. B **43**, 14363 (1991).
[34] V. Fiorentini, M. Methfessel, and M. Scheffler, Phys. Rev. Lett. **71**, 1051 (1993).
[35] J. A. Zimmerman, H. Gao, and F. F. Abraham, Modell. Simul. Mater. Sci. Eng. **8**, 103 (2000).
[36] S. Nosé, J. Chem. Phys. **81**, 511 (1984).
[37] W. G. Hoover, Phys. Rev. A **31**, 1695 (1985).
[38] S. J. Plimpton, J. Comput. Phys. **117**, 1 (1995).
[39] Computer code WARP, http://www.cs.sandia.gov/~sjplimp/lammps.html.
[40] M. F. Horstemeyer *et al.*, Sandia Technical Report No. SAND2001-8111, 2001 (unpublished).
[41] J. Diao, K. Gall, M. L. Dunn, and J. A. Zimmerman (unpublished).
[42] L. Lu, S. X. Li, and K. Lu, Scr. Mater. **45**, 1163 (2001).
[43] B. Wang, S. Yin, G. Wang, A. Buldum, and J. Zhao, Phys. Rev. Lett. **86**, 2046 (2001).
[44] V. Rodrigues and D. Ugarte, Nanotechnology **13**, 404 (2002).
[45] H. S. Park and J. A. Zimmerman (unpublished).
[46] A. F. Voter, F. Montalenti, and T. C. Germann, Annu. Rev. Mater. Sci. **32**, 321 (2002).